Synthesis of transmission line models for metamaterial slabs at optical frequencies

L. Fu,* H. Schweizer, H. Guo, N. Liu, and H. Giessen
4. Physikalisches Institut, Universität Stuttgart, D-70569 Stuttgart, Germany
(Received 24 September 2007; revised manuscript received 30 June 2008; published 10 September 2008)

We study the scattering parameters of typical transmission line resonant circuits and their corresponding nonlocal effective material parameters at optical frequencies using transmission line theory. We find that each circuit has specific features in terms of nonlocal permittivity and permeability and can be utilized to quantitatively synthesize transmission line circuit models for metamaterial slabs. As application examples, we construct circuit models for cut wires, cut-wire pairs, metallic meshes, and mesh pairs. Moreover, we calculate local material parameters in a simple way using fitted impedance parameters together with a transmission line homogenization procedure. Using transmission line (TL) models, we show how the material parameters can be optimized in actual metamaterials. The physical dependence of circuit parameters on structure geometries validates our TL model further.

DOI: 10.1103/PhysRevB.78.115110 PACS number(s): 41.20.Jb, 78.20.Ci, 78.67.−n, 84.40.Az

I. INTRODUCTION

Metamaterials are artificially designed media which consist of subwavelength structures for obtaining a specific electric and magnetic response. For instance, simultaneous negative permittivity and permeability in such a medium can result in a negative index of refraction.[1] Negative index materials are sometimes also called left-handed materials, because **E**, **H**, and **k** obey a left-hand tripod in some cases. These materials are of major research interest due to their potential applications for superlenses, compact cavity resonators, and other novel electromagnetic devices.[2–5] Negative permittivity generally exists in metals below the plasma frequency. In contrast, negative permeability is difficult to find in nature, especially in the optical regime. However, it can be achieved through metallic structure designs, such as split-ring resonators and cut-wire pairs.[6–8] A negative index of refraction was first experimentally demonstrated at gigahertz frequencies.[9] Recently, fabrication progress has enabled the realization of a negative index in the near-infrared and visible spectral ranges[8,10–12] and the realization of three-dimensional (3D) metamaterials at optical frequencies.[13]

Transmission line (TL) theory is of significant importance for the design and analysis of microwave networks. Theoretical treatments showed that scattering problems of geometrically discontinuous metallic structures with subwavelength dimensions can be viewed as lumped elements which are distributed in a TL circuit.[14] Circuit models for inductive metallic meshes and capacitive metallic plates (or equivalently, capacitive meshes or cut wires as in this work) in filter designs at far-infrared frequencies were extensively studied.[15–17] TL theory was successfully employed in designing one-, two-, or three-dimensional metamaterials at gigahertz frequencies.[18–22] In a homogenous TL, the effective permittivity and permeability have straightforward relations with discrete lumped elements, which facilitate the understanding and optimization of metamaterials. That is, the magnetic permeability μ is represented by a series per unit length impedance, i.e., $Z'=j\omega\mu=j\omega\mu_0\mu_r$, while the electric permittivity ε is represented by a shunt per unit length admittance, i.e., $Y'=j\omega\varepsilon=j\omega\varepsilon_0\varepsilon_r$.[18,23] Recently it was demonstrated that the electrical engineering concept of circuit models can be transferred to optical metamaterials.[24–31] Furthermore, it was demonstrated that by joining together arrays of nanocircuits of nanoparticles, two- or three-dimensional TL optical metamaterials can be obtained to support forward or backward electromagnetic waves.[25–27] These studies were carried out mainly on nanoscale particles with positive or negative permittivities. The circuit models were also obtained through an *analytical* quasistatic approach, which are quite difficult to obtain for complicated structures. It is not clear yet which kind of TL equivalent circuit a conventional optical metamaterial possesses, or how we can synthesize an appropriate TL circuit model for a more complicated structure in a general way. The obtained circuit models may serve as alternative building blocks for nano-TL metamaterials.

In this paper, a general method for quantitatively synthesizing TL circuit models for metamaterial slabs is suggested. We start with three typical two-port TL resonant circuits without direct connection to any metamaterial. Scattering (S) parameters of the circuits are calculated using TL equations, and the nonlocal effective material parameters (ε_{rN} and μ_{rN}) are extracted.[32–35] We find that each circuit is related to specific features of the extracted ε_{rN} and μ_{rN} spectra. By careful analysis of these material parameters of a metamaterial, an appropriate TL circuit model can be constructed. Although the impedance and the refractive index are the most relevant material parameters and indeed are the physical ones, the nonlocal material parameters obtained using this simple procedure can result in clear signatures of the corresponding circuit.

In fact, the effective material parameters extracted or retrieved from the Fresnel-Airy expressions[32–35] are nonlocal (see Refs. 36–39 and references therein). In some regions they might even show a nonphysical behavior near the Bragg mode. Various approaches to studying local material parameters of metamaterials have been performed,[36,40–42] from which no simple and straightforward procedure is available. In this report, a different approach for local material parameters is used. First, the nonlocal material parameters, which are extracted in a simple way, are utilized as an aid to construct TL circuit models. In turn, local and physical material parameters are calculated using the fitted element parameters

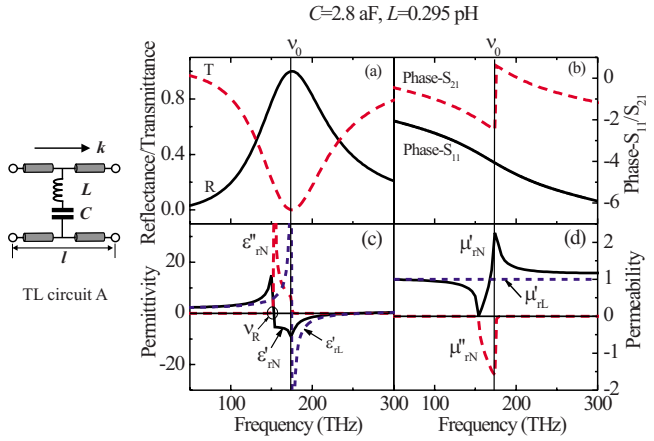

FIG. 1. (Color online) Circuit A is a dimensionless shunt admittance composed of a series combination of L and C loading a TL section of length l at its center. (a), (b), (c), and (d) show the calculated frequency-dependent reflectance (solid line)/transmittance (dashed line), phase S_{11} (solid line)/S_{21} (dashed line), retrieved permittivity, and permeability, respectively. The short-dashed line in (c) is calculated using Eq. (2), a TL homogenization procedure.

of the constructed TL circuit model and a TL homogenization procedure. Moreover, we show that the nonlocal material parameters can still qualitatively describe the real electromagnetic response of metamaterial slabs outside of the Bragg mode region.

We have to emphasize that the synthesized models are only appropriate for the slabs at the defined polarization and at normal incidence. The circuit geometry might be the same when the polarization is changed. This is the case for all the examples shown in this report. However, the values of L and C have to be changed, correspondingly. If the slabs are stacked, the circuit remains similar only when the interaction between the slabs can be neglected. This is especially valid for Bloch lattices.[37]

This paper is arranged as follows: First, S parameters and retrieved nonlocal material parameters of three typical TL circuits are calculated and presented in Sec. II. Local material parameters using the TL homogenization procedure are presented and compared with their nonlocal counterparts. Procedures for using numerical simulation results of the optical metallic structures to synthesize their corresponding TL models are shown in Sec. III. Discussions about how to apply TL models to optimize actual metamaterials are presented. The dependence of circuit parameters on structure geometries in cut-wire pairs is studied to improve our understanding of this structure.

II. TRANSMISSION LINE CIRCUITS AND THEIR NONLOCAL EFFECTIVE MATERIAL PARAMETERS

To transfer the electrical engineering TL theory in the microwave regime into the optical regime, we are first going to consider three typical TL circuit models, one of which is shown in Fig. 1(a). The electromagnetic wave propagates along the TL with a propagation constant k. According to TL theory, all the circuit elements can be described by $ABCD$ matrices. The $ABCD$ matrix of a system consisting of cascaded elements is just the multiplication of the individual matrices. The global $ABCD$ matrix can then be converted into S parameters and measurable reflectance and transmittance.[43] In our models under study, lumped elements are dimensionless, which is a good approximation for thin metallic slabs.[44] In contrast, a section of a TL is an element exhibiting a physical length l.

In analyzing these circuits at optical frequencies, their resonances are set to be around 200 THz, which is determined by $\nu_0 = 1/2\pi\sqrt{LC}$. For a given amount of loss, the bandwidth is determined by the ratio L/C.[43] An arbitrary TL section is added at each end of the loads, which leads to a total length l. In this report, $l = 260$ nm is employed. To avoid singularities in the calculation, a small resistance of 0.001 Ω is added in series with L (which accounts for an optical loss, as we will show in Sec. II A). We do not display this resistance in the figures in this section for reason of clarity.

To obtain the nonlocal effective μ_{rN} and ε_{rN} of a TL system or a metamaterial slab, a retrieval procedure based on scattering coefficients is used.[32,33] First, the impedance Z is calculated from the scattering coefficient. Then, the single-pass transmission coefficient of the system is calculated, from which the effective index n_{eff} is extracted directly. Finally, μ_{rN} and ε_{rN} are obtained using the relationships $\mu_{rN} = Zn_{\text{eff}}$ and $\varepsilon_{rN} = n_{\text{eff}}/Z$.

A. Analysis of TL circuit A

The schematic of the first circuit (A) is shown in Fig. 1. It is a dimensionless shunt admittance composed of a series combination of a capacitance and an inductance, loading a TL section of length l (vacuum) at its center. The parameters of L and C for the calculation are given in the caption. Figures 1(a)–1(d) show the calculated frequency-dependent reflectance/transmittance, scattering-parameter phase, and retrieved permittivity ($\varepsilon_{rN} = \varepsilon'_{rN} + j\varepsilon''_{rN}$) and permeability ($\mu_{rN} = \mu'_{rN} + j\mu''_{rN}$). Circuit A is a stop band element,[43] exhibiting a band-rejection resonant behavior and a π jump on phase S_{21} at ν_0. In addition, the real part of the effective permittivity ε'_{rN} displays a resonant behavior, and the real part of the effective permeability μ'_{rN} displays an antiresonant behavior, which resemble those of cut-wire metamaterials,[45] although no concrete material structure is involved in this analysis. The resonance frequency ν_0 corresponds to a minimum and a maximum on the ε'_{rN} and μ'_{rN}, respectively. Simultaneously, ε''_{rN} is positive and its maximum is at ν_R, at which ε'_{rN} is zero. Since $n_{\text{eff}} = \sqrt{\varepsilon_{rN}\mu_{rN}}$ is finite, μ'_{rN} necessarily is zero at this frequency. In addition, μ''_{rN} is negative with its minimum at ν_0, at which μ'_{rN} achieves its maximum.

The above displayed μ''_{rN} has a negative sign around ν_0, which is nonphysical and will be discussed later. Yet the physical material parameters can be calculated using the TL homogenization procedure through the simple relation $Y' = Y/l = j\omega\varepsilon = j\omega\varepsilon_0\varepsilon_r$ for homogenous materials, where Y' is the per unit length admittance of the TL section. For circuit A in Fig. 1, we obtain[46]

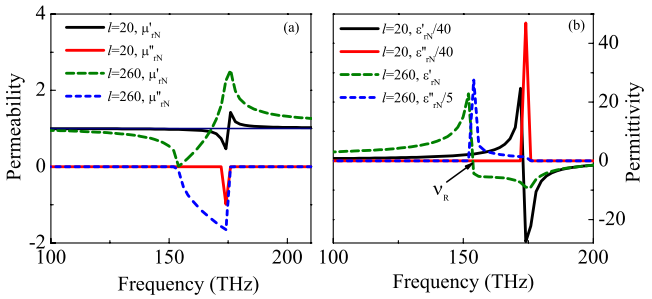

FIG. 2. (Color online) Influence of the TL-section length l on the extracted effective μ_{rN} (a) and ε_{rN} (b). A shorter TL section reduces the nonphysical region (induced by the Bragg mode) of μ'_{rN}, which resembles μ'_{rL} more, a unit constant.

$$Y' = \frac{Y}{l} = \frac{Y_{\mathrm{TL}} + Y_{\mathrm{disc}}}{l}, \tag{1}$$

where $Y_{\mathrm{TL}} = j\omega C_0 = j\omega\varepsilon_0 l$ is the admittance of the TL section and $Y_{\mathrm{disc}} = 1/(j\omega L + R + 1/j\omega C)$ is the admittance of the discontinuity. Hence, the permittivity for a homogenized medium can be calculated as

$$\varepsilon_{rL} = 1 - \left(\frac{1}{\varepsilon_0 l}\right)\frac{C\omega_0^2}{\omega^2 - \omega_0^2 - j\omega RC\omega_0^2}, \tag{2}$$

where $\omega_0 = 2\pi\nu_0$. ε'_{rL} has a Lorentz type dispersion and its curve is shown as the short-dashed line in Fig. 1(c). This homogenization procedure is equivalent to the calculation of local material parameters using electric or magnetic polarizabilities,[36] which are directly connected to Y and Z for Bloch lattices.[37]

The negative sign of μ''_{rN} around the resonance frequency violates the passivity condition and is induced due to a spatial lattice resonance (Bragg resonance).[36] It can be revealed from the fact that decreasing the TL-section length causes a diminishing imaginary part with negative sign. As shown in Fig. 2, when l is changed from 260 to 20 nm, the frequency range with negative μ''_{rN} becomes narrower and the amplitude of μ'_{rN} approaches unity. At the same time, the shape of ε'_{rN} approaches that of ε'_{rL}, and ν_R shifts toward ν_0. However, outside the nonphysical region, both at the high-frequency side and at the far low-frequency side of ν_0, ε_{rN} describes the behavior of ε_{rL} well.

B. Analysis of TL circuit B

The bandpass building block of circuit B is shown in Fig. 3.[43] It is a dimensionless shunt admittance composed of a parallel combination of a capacitance and an inductance loading a TL section with length l at its center. The parameters of L and C for the calculation are given in the caption. Figures 3(a)–3(d) show the calculated frequency-dependent reflectance/transmittance, scattering-parameter phase, retrieved permittivity, and permeability, respectively.

In this circuit, the shapes of the frequency-dependent reflectance/transmittance are exchanged with respect to those in Fig. 1, and the circuit exhibits a bandpass behavior. In addition, a π jump occurs on phase S_{11} at the resonance

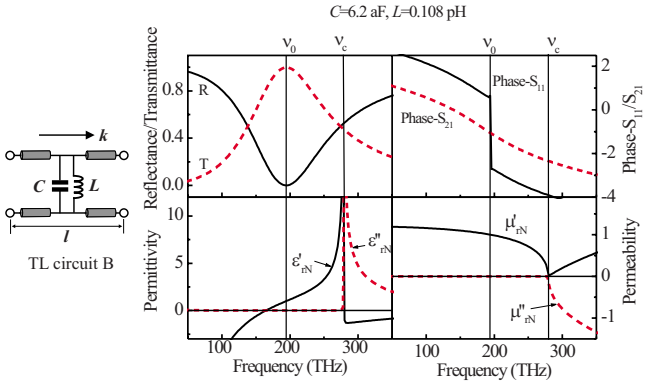

FIG. 3. (Color online) Circuit B is a dimensionless shunt admittance composed of a parallel combination of a capacitance and an inductance loading a TL section of length l at its center. (a), (b), (c), and (d) show the calculated frequency-dependent reflectance (solid line)/transmittance (dashed line), scattering-parameter phase, retrieved permittivity, and permeability (dashed lines for the imaginary parts), respectively.

frequency ν_0. However, ε_{rN} displays a resonance at ν_c. In a broad low-frequency range, ε'_{rN} is negative, as in bulk metals. In contrast, ν_c corresponds to a minimum of μ'_{rN}, and μ''_{rN} becomes negative at the high-frequency side. The resonance of ε_{rN} can be also attributed to the Bragg mode. This is confirmed by the calculation that upon decreasing the TL-section length, ν_c shifts toward higher frequencies, and the negative ε_{rN} at the low-frequency side becomes broader.

C. Analysis of TL circuit C

The stop band building block of circuit C is shown in Fig. 4. It is a dimensionless series impedance composed of a parallel combination of a capacitance and an inductance, loading a TL section of length l at its center. Figures 4(a)–4(d) show the calculated frequency-dependent reflectance/transmittance, scattering-parameter phase, retrieved permittivity, and permeability, respectively.

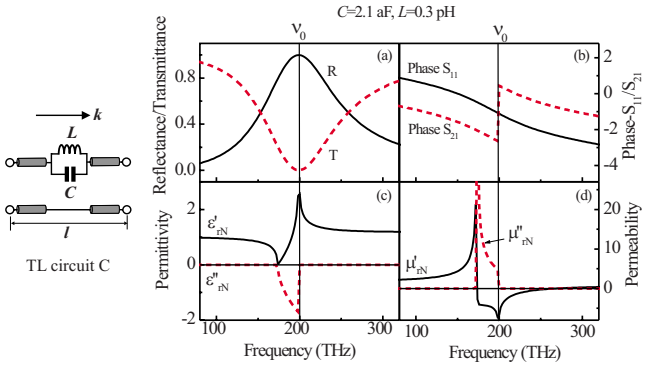

FIG. 4. (Color online) Circuit C is a dimensionless series impedance composed of a parallel combination of a capacitance and an inductance loading a TL section of length l at its center. (a), (b), (c), and (d) shows the calculated frequency-dependent reflectance (solid line)/transmittance (dashed line), scattering-parameter phase, retrieved permittivity, and permeability (dashed lines for the imaginary parts), respectively.

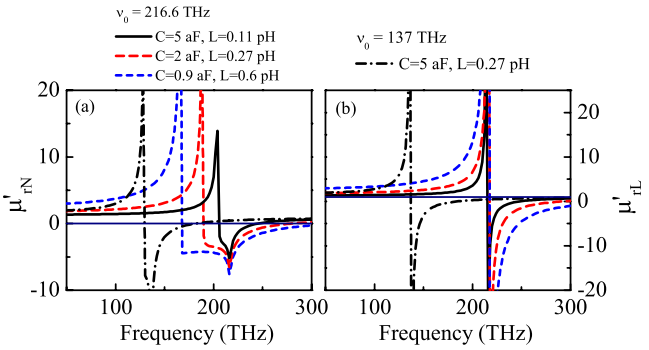

FIG. 5. (Color online) Frequency-dependent μ'_{rN} (a) and μ'_{rL} (b) for circuit C with varying values of L and C.

The frequency-dependent reflectance and transmittance take exactly the same shapes as those of circuit A shown in Fig. 1(a). Similarly, a π jump occurs also at ν_0 on phase S_{21}. Nevertheless, phase S_{11} has an overall phase shift of π compared to that of circuit A. The similarity between these two circuits makes it difficult to distinguish them only from phase change or reflectance/transmittance spectra, especially for a metamaterial with a complicated circuit combination. However, the retrieved material parameters display clear features of the circuit with interchanged shapes as the ones shown in Figs. 1(c) and 1(d). Namely, ε'_{rN} has an antiresonant behavior and μ'_{rN} has a resonant behavior,[45] whereas ε''_{rN} is negative and μ''_{rN} is positive. In addition, ε'_{rN} shows a maximum and μ'_{rN} shows a minimum at ν_0. Likewise, the negative sign of ε''_{rN} can be attributed to the Bragg mode.

Similar to ε'_{rL} for circuit A, the simple relation of $Z' = Z/l = j\omega\mu = j\omega\mu_0\mu_r$ for homogeneous media can yield the local μ_{rL} with a Lorentz dispersion:

$$\mu_{rL} = 1 - \left(\frac{1}{\mu_0 l}\right)\frac{\omega_0^2(L - jR/\omega)}{\omega^2 - \omega_0^2 - j\omega RC\omega_0^2}. \tag{3}$$

A negative μ'_{rN} or μ'_{rL} is achieved in this circuit, owing to the existence of the series C. It was used to model the magnetic resonance in split-ring resonator based negative index metamaterials.[46] Of particular interest is how the bandwidth of the negative μ'_{rN} or μ'_{rL} can be increased. For this aim, the ratio of L to C is first varied without modifying the resonant frequency. The results of μ'_{rN} are shown in Fig. 5(a) for three values of C given in the inset with constant $\nu_0 = 216.6$ THz. With smaller C, both the resonance and the frequency range with negative μ'_{rN} becomes broader. However, when L is increased without changing C, the negative amplitude of μ'_{rN} becomes larger. This is obvious when comparing the solid line with the dash-dotted line in Fig. 5(a). To validate this tendency, the local permeability μ'_{rL} is also calculated correspondingly and plotted in Fig. 5(b). The same behavior of μ'_{rL} with varying C and L is observed, especially in the region with $\nu > \nu_0$. Both calculations reveal that the series C has to be decreased in order to obtain a broadband negative permeability. To obtain a larger amplitude, the series L has to be increased.

The analysis above demonstrates that every circuit has its own specific nonlocal effective ε_{rN} and μ_{rN} responses in terms of resonant or antiresonant behavior, curve shapes, sign of the imaginary parts, and extremum frequency. Therefore, these responses can be viewed as signatures of the corresponding circuit and can be used to synthesize TL models for metamaterials as shown in Sec. III. Although there are still many other combination possibilities of lumped L and C in the TL, similar analysis methods may be applied.

III. OPTICAL METAMATERIALS AND THEIR TRANSMISSION LINE MODELS

In this section, TL models for several optical metamaterials including periodic cut wires, cut-wire pairs, metallic meshes, and mesh pairs are synthesized based on numerical results and retrieved nonlocal effective material parameters. The metallic structures are situated in vacuum and arranged periodically in two dimensions on a single plane. The length of the unit cell along the k direction is $l = 260$ nm, corresponding to l in the TL circuits. The structure dimensions are chosen so that they have roughly the same resonance frequency and bandwidth as the TL circuits discussed in Sec. II. The metal is silver with a thickness of 20 nm. A Drude model was used to describe the dispersion of its permittivity, with a plasma frequency of 1.37×10^{16} Hz and a scattering frequency of 8.5×10^{13} Hz.[12] The electromagnetic wave response (S parameters) of the structures including four unit cells was simulated in a waveguide geometry using CST MICROWAVE STUDIO,[47] which is based on a finite integration time-domain algorithm. Light is incident normally upon the structure with an electric field along the x direction and a magnetic field along the y direction. When it is incident at oblique angles, the corresponding TL model might be changed. The structures studied here are termed "frequency selective surfaces," from the viewpoint of electrical engineering.[48] However, the name *metamaterial* has been widely accepted for such structures in the optical regime.[7,10,11] Volumetric 3D metamaterials are currently not

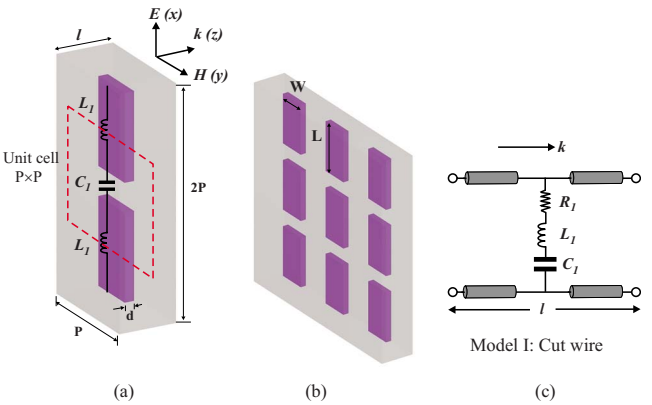

FIG. 6. (Color online) (a) Two cut-wire unit cells demonstrate the interactions at the defined polarization. (b) Overall structure of the 2D periodic Ag cut-wire array (purple blocks) in vacuum (gray block). (c) Circuit model for both the unit cell and the overall structure, which is identical to circuit A shown in Fig. 1. The structure parameters are $L = 500$ nm, $W = 150$ nm, $d = 20$ nm, and $P = 600$ nm. The E field is along the length of the wires.

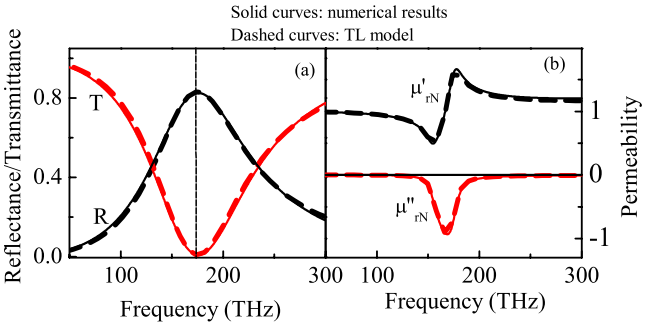

FIG. 7. (Color online) (a) Frequency-dependent reflectance/transmittance and (b) the retrieved permeability from numerical simulation (solid curves) and TL calculation using model I (dashed curves) for the structures shown in Fig. 6. The circuit parameters are tabulated in Table I.

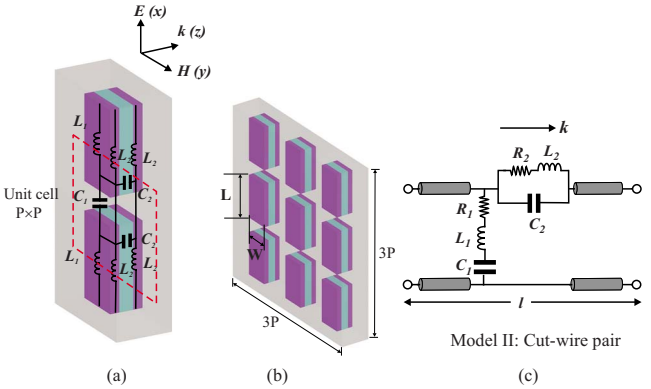

FIG. 8. (Color online) (a) Two cut-wire-pair unit cells to show the interaction at the defined polarization. (b) Overall structure of the 2D periodic Ag cut-wire-pair array in vacuum. (c) Circuit model for both the unit cell and the overall structure, which is a combination of circuits A and B. The geometry of the cut wires is the same as that in Fig. 6. The spacer between the cut-wire pairs is 60-nm-thick vacuum (dark blue). The E field is along the length of the wires.

available but are possible from both technological and theoretical points of view.[13,26,49]

To see how well the constructed circuit models can describe the corresponding structures, S parameters of the models are calculated using the parameters of L and C which were obtained by fitting the numerical results. The fitting procedure is unique, with the LC product determining the resonance frequency and the L/C ratio determining the resonance width. A resistance R is implemented to describe optical losses. This influences mainly the reflectance and transmittance amplitude. R is assumed to be always in series with the inductance due to the flow of the induced current.

A. TL models for cut wires and cut-wire pairs

Figure 6(b) shows a schematic of a two-dimensional (2D) periodic cut-wire array. The structure has a period of 600 nm in both the x and the y directions. A single cut wire has a length of $L=500$ nm and a width of $W=150$ nm. The E field is along the length of the wires. Numerical results of the frequency-dependent reflectance/transmittance and the effective permeability are displayed in Fig. 7 as solid curves.

The features of these curves are similar to those shown in Fig. 1. Namely, this structure exhibits a band-rejection behavior, and μ'_{rN} exhibits an antiresonant behavior, similar to the cut wires at gigahertz frequencies.[45] Also, the features of phase S_{21} and ε'_{rN} are the same as those in Fig. 1 but are not shown here for brevity. The retrieved permeability is somewhat rounded in the simulated structure, which is induced by the scattering loss defined by the metal dispersion. Therefore, circuit A is used directly to model the cut wires as shown in Fig. 6(c) and renamed as model I. Using the values of L_1, C_1, and R_1 tabulated in Table I, the calculated spectra of model I can reproduce the numerical results very well, as shown by the dashed curves in Fig. 7. Furthermore, model I is also identical to that of the capacitive plates at far-infrared frequencies.[15] However, it is obtained here in a different way.

Cut-wire pairs were studied in view of their potential for negative μ'_{rN} (Refs. 7 and 50) and negative index of refraction.[8] Figure 8 shows the schematic of a 2D periodic cut-wire-pair array. The whole structure is still situated in vacuum, and all other structure parameters are the same as for one layer. The two layers are separated by a vacuum spacer with a thickness of $d_s=60$ nm. Numerical results of S parameters and retrieved μ'_{rN} of the structure are shown in Figs. 9(a) and 9(b) as solid curves. Two resonances of μ'_{rN} are shown, one being the resonant mode and the other being the antiresonant mode, which take the shapes shown in Figs. 4(d) and 1(d), respectively. Furthermore, the minimum of the resonant mode ν_2 and the maximum of the antiresonant mode ν_1 correspond to two minima of the transmittance curve. ε'_{rN} behaves also correspondingly to μ'_{rN} as discussed in Sec. II (not shown here). Thus, the TL model for the cut-wire pairs is constructed by combining circuit A (composed of R_1, L_1, and C_1) and circuit C (composed of R_2, L_2, and C_2) as shown in Fig. 8(c). Circuit model II is a dual composite right-/left-handed transmission line, which can

TABLE I. Circuit parameters for calculating the electromagnetic response of the TL models.

Model	L_1 (pH)	C_1 (aF)	R_1 (Ω)	L_2 (pH)	C_2 (aF)	R_2 (Ω)
I	0.295	2.8	18.0			
II	0.169	3.8	2.5	0.018	61	0.5
III	0.148	3.12	8.0	0.063		7.0
IV	0.055	11.0	1.1	0.0245	21.0	0.5

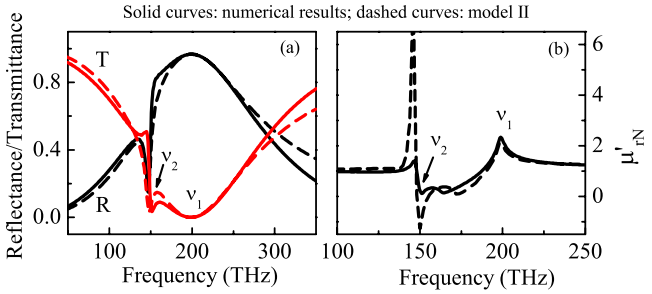

FIG. 9. (Color online) Frequency-dependent S parameters and retrieved μ'_{rN} from numerical simulation (solid curves) and TL calculation (dashed curves) for the cut-wire pairs shown in Fig. 8 with d_s=60 nm.

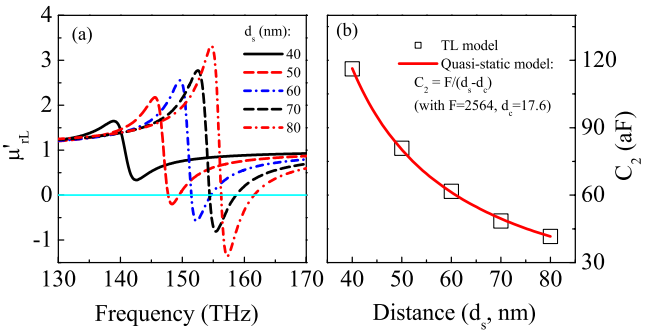

FIG. 10. (Color online) Frequency-dependent μ'_{rL} of cut-wire pairs shown in Fig. 8 with varied spacer thickness d_s. (b) Series capacitance C_2 versus spacer thickness of cut-wire pairs (scattered data), which can be well understood by using the quasistatic model for a parallel capacitor (solid line).

yield a left-handed band with broad bandwidth with properly matched L and C in a homogenous network.[51]

The circuit parameters of model II obtained through fitting the numerical S parameters are listed in Table I. Although there are six free parameters, the transmittance resonance dip positions ν_1 and ν_2, the bandwidths, and the amplitudes of the resonances are fixed. Therefore, the fitted parameters are unique.

Calculated responses of the model are displayed by the dashed curves in Fig. 9, which agree well with the numerical results. However, the amplitude of μ'_{rN} deviates from the numerical result around ν_2. This is due to the assumption that all of the lumped elements are situated on one junction plane in our TL model. This assumption holds well for one layer cut wires, because the elements originate only from the lateral interactions of the metals on one plane. However, with two layers and with longitudinal interactions along the TL which result in the series elements, distributed TL should be used. For instance, with a Π-type TL model, better agreement of the S parameters with those simulated can be obtained. However, the simplified model provides us a clear overview.

A smaller series capacitance would result in a broader negative μ'_{rL}, as has been discussed for circuit C shown in Fig. 5. For a classical parallel plate capacitor, a larger plate distance would lead to a smaller capacitance. To see if the classical model can still be applied to cut-wire pairs, the structure is further simulated with varied spacer thickness d_s and fixed physical length l=260 nm. Through fitting the Π-type TL model to simulated S parameters, the values of L_2, C_2, and R_2 are obtained. The calculated local permeability μ'_{rL} is plotted in Fig. 10(a) for different d_s. The dependence of C_2 on d_s is plotted in Fig. 10(b). With increased d_s, both the amplitude and the bandwidth of the negative μ'_{rL} is increased. Correspondingly, the series capacitance C_2 is decreased with increased d_s, which confirms our prediction. Furthermore, the relationship of C_2 with d_s can be well understood using the quasistatic model shown in the inset of Fig. 10(b), in which both F and d_c are fitting parameters, and further validates our TL model. It turns out that TL models provide us with the possibility of deriving a quantitative relationship of circuit elements with structure geometry parameters.

B. TL models for metallic meshes and mesh pairs

A schematic for a metallic mesh is shown in Fig. 11. It is the Babinet complementary structure[15,52] of the cut wires shown in Fig. 6, with W=150 nm, L=500 nm, and P=600 nm. Numerical results are displayed as solid curves in Fig. 12. In contrast to the cut wires, the mesh structure shows a bandpass behavior with the same resonance frequency and a comparable bandwidth. First, by incorporating an additional resistance, TL circuit B in Fig. 3 is used to model the structure, which is identical to the one used in Ref. 15. The calculated results are plotted as dotted curves in Figs. 12(a)–12(d). It is rather difficult to fit the numerical results at the high-frequency side of the resonance, which leads to a larger deviation from the numerical results of both the S parameters and the effective material parameters.

Figure 12(d) reveals that the retrieved μ'_{rN} (solid line) is composed of two resonant types in the studied frequency range: One is antiresonant, taking the form of circuit B, and the other one is resonant, assuming the form of circuit A. The model for the mesh is therefore constructed by combining

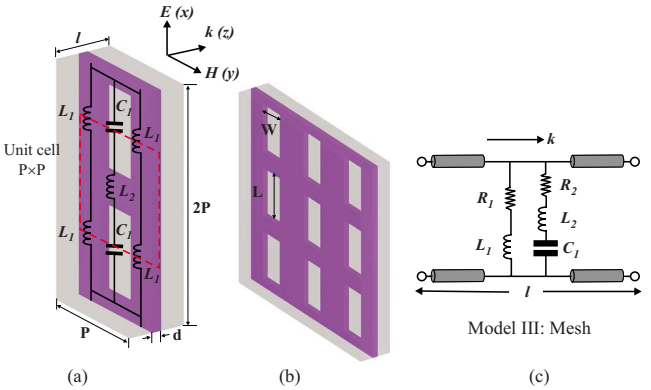

FIG. 11. (Color online) (a) Two unit cells of the mesh to show the interaction at the defined polarization. (b) Overall structure of the 2D periodic Ag grid (gray) in vacuum. (c) Circuit model for both the unit cell and the overall structure, which is a combination of circuits B and A. The E field is along the x direction. The geometry parameters are W=150 nm, L=500 nm, d=20 nm, and P=600 nm.

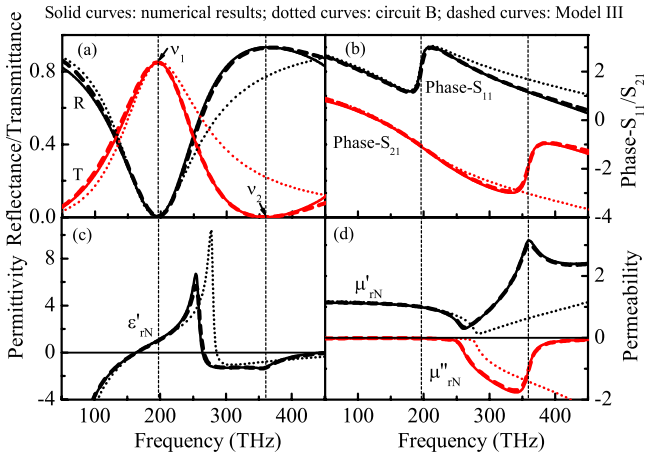

FIG. 12. (Color online) Reflectance/transmittance, S-parameter phase, and recovered material parameters from numerical simulations (solid curves) of the mesh structure and TL calculations using circuit B alone (dotted curves) and using model III shown in Fig. 11 (dashed curves). The vertical dashed guide lines indicate the phase-jump frequencies.

the two into model III as demonstrated in Fig. 11(c), with R_1, L_1, and partially C_1 from circuit B and R_2, L_2, and partially C_1 from circuit A. The calculated results of the model are shown as dashed curves in Fig. 12 and were obtained using the parameters of the lumped elements tabulated in Table I. Both the numerical S parameters and the retrieved material parameters can be very well reproduced. The two resonances correspond to $\nu_1 = 1/\pi\sqrt{(L_1+L_2)C_1}$ and $\nu_2 = 1/\pi\sqrt{L_2 C_1}$. Model III indicates that the TL model of the Babinet structure of cut wires can be represented by the model for cut wires shunted by an inductance. It also gives an intuitive understanding of the structure: L_1 stems from the induced current in the long wire along the E field in the x direction, and L_2 is caused by the wire perpendicular to the E field, but the current is still along the x direction. On the other hand C stems from the holes where charges can accumulate.

Similarly, the mesh is replicated along the k direction with a distance of 60 nm to obtain a mesh pair as shown in Fig. 13. Numerical results are shown in Fig. 14. Using a similar

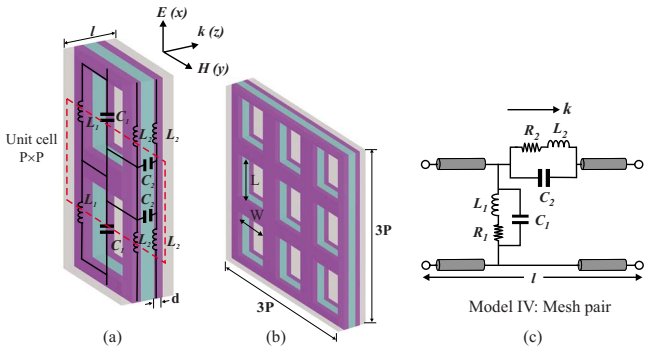

FIG. 13. (Color online) (a) Two unit cells of mesh pairs and the interaction between them at the defined polarization. (b) Overall structure of the 2D periodic metallic mesh-pair array in vacuum. (c) Circuit model for both the unit cell and the overall structure. The E field is along the x direction.

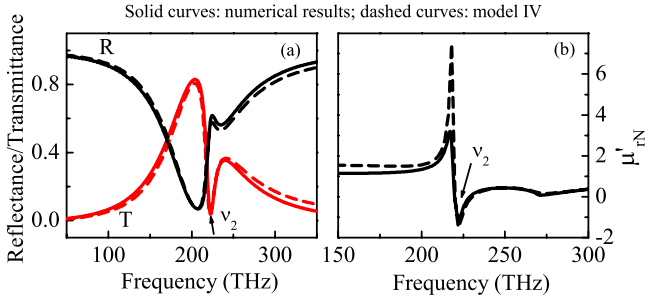

FIG. 14. (Color online) S parameters and the recovered material parameters from numerical simulation (solid curves) of the mesh-pair structure and TL calculation (dashed curves) using model IV shown in Fig. 13.

procedure, model IV for a mesh pair is constructed using a combination of circuit B (R_1, L_1, and C_1) and circuit C (R_2, L_2, and C_2). The properties of the model are calculated using the parameters given in Table I. Good agreement with the numerical results is obtained, as demonstrated by the dashed curves in Fig. 14. Apparently, due to the longitudinal coupling, the shunt L_2 in Fig. 11 is transformed into series L_2 and C_2. As in the cut-wire-pair case, the series capacitance C_2 is responsible for the negative μ'_{rN} at ν_2. With optimized geometrical parameters, a negative index in a mesh pair can be obtained[10,12] due to the coexistence of a series C_2 and a shunt L_1. Comparing it with its complementary structure of the cut-wire pairs, the mesh pair has a larger L_2 and a smaller C_2 as shown in Table I, which are favorable for producing a broader negative permeability.

To further clarify the difference between the cut-wire pairs and the mesh pairs, local material parameters for the two structures are calculated using Eq. (1) for ε_{rL} and Eq. (3) for μ_{rL}, and are compared in Fig. 15. Both ε'_{rL} and $\mu_{rL'}$ of the cut-wire pairs have a Lorentz response. To tune their negative parts into the same frequency range is rather difficult, especially when μ'_{rL} has only a small negative amplitude or exists only over a narrow frequency range. On the contrary, the mesh-pair structure possesses a broadband negative permittivity and a negative μ'_{rL} with a relative large amplitude, which makes this structure feasible for obtaining a negative index with different geometries or structure parameters.[10,12,53,54] Similar to the optimization procedure with cut-wire pairs, we would expect a decreased series ca-

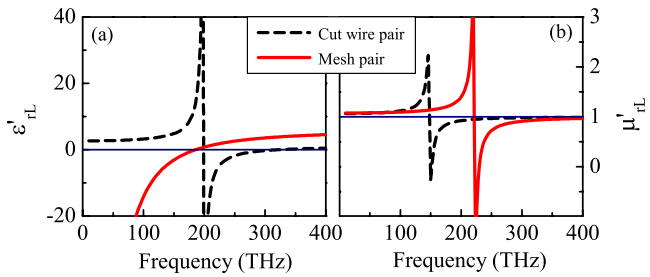

FIG. 15. (Color online) Local material parameters of cut-wire pairs and mesh pairs calculated using the TL models II and IV and the fitted circuit element parameters listed in Table I. (a) Real parts of the local permittivity and (b) real parts of the local permeability.

pacitance C_2 in model IV and a broader negative permeability through increasing the distance between the mesh pairs. Further studies concerning the dependence of circuit parameters on structure geometries would yield better understanding of metamaterials and will be given in a separate paper.

IV. CONCLUSION

Three typical transmission line circuits have been studied using TL theory. Each circuit exhibits specific responses in terms of its nonlocal effective material parameters, which are extracted using a simple procedure. These parameters are used to conveniently construct TL models for planar optical metamaterials. Our method has been applied to cut wires (capacitive plates), cut-wire pairs, metallic meshes, and mesh pairs at optical frequencies. The constructed models are validated by the good agreement of reflectance/transmittance spectra and nonlocal material parameters with simulations.

It has been further demonstrated that using the synthesized circuit models, local material parameters can be calculated in turn. This is equivalent to saying that first the impedances of the metamaterials are determined, then their electromagnetic response is averaged along the TL section as in Ref. 37. On the contrary, in the extraction procedure for nonlocal material parameters, the wave propagation in vacuum is taken as a part of the electromagnetic response of the metamaterial, which induces nonphysical and nonlocal material parameters.[36] However, the nonlocal material parameters can still describe the electromagnetic response away from the Bragg mode qualitatively.

Employing these circuit models, a physical insight into optical metamaterials was obtained: We have clarified why a negative index in mesh pairs is easier to obtain than in its complementary structure of cut-wire pairs. We have demonstrated how to optimize the negative permeability in cut-wire pairs in terms of bandwidth and amplitude. We have obtained a quantitative dependence of the series capacitance with one of the structure geometries in cut-wire pairs, which can be well described using a quasistatic model. This demonstrates that our TL model can be used to quantitatively analyze metamaterials. When the interaction between stacked slabs of metamaterials can be neglected, they are in the Bloch lattice regime.[37] Then the constructed models may be used as building blocks for 3D optical metamaterials.[27]

ACKNOWLEDGMENTS

We would like to thank C. Simovski and T. Meyrath for many helpful discussions. We acknowledge the support from DFG (Grants No. Schw470-19 and No. FOR557), BMBF (Grant No. 13N9155), and Landesstifung BW.

*l.fu@physik.uni-stuttgart.de

[1] V. G. Veselago, Sov. Phys. Usp. **10**, 509 (1968).
[2] J. B. Pendry, Phys. Rev. Lett. **85**, 3966 (2000).
[3] J. B. Pendry, D. Schurig, and D. R. Smith, Science **312**, 1780 (2006).
[4] V. M. Shalaev, Nat. Photonics **1**, 41 (2007).
[5] N. Engheta, IEEE Antennas Wireless Propag. Lett. **1**, 10 (2002).
[6] J. B. Pendry, A. J. Holden, D. J. Robbins, and W. J. Stewart, IEEE Trans. Microwave Theory Tech. **47**, 2075 (1999).
[7] G. Dolling, C. Enkrich, M. Wegener, J. Zhou, C. M. Soukoulis, and S. Linden, Opt. Lett. **30**, 3198 (2005).
[8] V. M. Shalaev, W. Cai, U. K. Chettiar, H. K. Yuan, A. K. Sarychev, V. P. Drachev, and A. V. Kildishev, Opt. Lett. **30**, 3356 (2005).
[9] R. A. Shelby, D. R. Smith, and S. Schultz, Science **292**, 77 (2001).
[10] S. Zhang, W. Fan, K. J. Malloy, and S. R. J. Brueck, Opt. Express **13**, 4922 (2005).
[11] S. Zhang, W. Fan, K. J. Malloy, and S. R. J. Brueck, J. Opt. Soc. Am. B **23**, 434 (2006).
[12] G. Dolling, C. Enkrich, M. Wegner, C. M. Soukoulis, and S. Linden, Opt. Lett. **31**, 1800 (2006).
[13] N. Liu, H. Guo, L. Fu, S. Kaiser, H. Schweizer, and H. Giessen, Nat. Mater. **7**, 31 (2008).
[14] N. Marcuvitz and J. Schwinger, J. Appl. Phys. **22**, 806 (1951).
[15] R. Ulrich, Infrared Phys. **7**, 37 (1967).
[16] D. H. Dawes, R. C. McPhedran, and L. B. Whitbourn, Appl. Opt. **28**, 3498 (1989).
[17] K. D. Moeller, O. Sternberg, H. Grebel, and K. P. Stewart, Appl. Opt. **41**, 1942 (2002).
[18] G. V. Eleftheriades, A. K. Iyer, and P. C. Kramer, IEEE Trans. Microwave Theory Tech. **50**, 2702 (2002).
[19] C. Caloz and T. Itoh, IEEE Trans. Antennas Propag. **52**, 1159 (2004).
[20] P. Alitalo, S. Maslovski, and S. Tretyakov, J. Appl. Phys. **99**, 064912 (2006).
[21] M. Zedler, P. Russer, and C. Caloz, Proceedings of the IEEE MTT-S International Microwave Symposium Digest, Honolulu, HI, 2007 (unpublished), p. 1827.
[22] A. K. Iyer and G. V. Eleftheriades, IEEE Trans. Antennas Propag. **55**, 2746 (2007).
[23] C. Caloz and T. Itoh, Proceedings of the IEEE AP-S International Symposium USNC/URSI National Radio Science Meeting, San Antonio, TX, 2002 (unpublished), p. 412.
[24] N. Engheta, A. Salandrino, and A. Alù, Phys. Rev. Lett. **95**, 095504 (2005).
[25] A. Alù and N. Engheta, J. Opt. Soc. Am. B **23**, 571 (2006).
[26] A. Alù and N. Engheta, Phys. Rev. B **75**, 024304 (2007).
[27] N. Engheta, Science **317**, 1698 (2007).
[28] T. P. Meyrath, T. Zentgraf, and H. Giessen, Phys. Rev. B **75**, 205102 (2007).
[29] S. Tretyakov, Metamaterials **1**, 40 (2007).
[30] L. Fu, H. Schweizer, H. Guo, N. Liu, and H. Giessen, Appl. Phys. B: Lasers Opt. **86**, 425 (2007).
[31] H. Schweizer, L. Fu, H. Guo, N. Liu, and H. Giessen, Phys. Status Solidi B **244**, 1243 (2007).
[32] A. M. Nicolson and G. F. Ross, IEEE Trans. Instrum. Meas. **19**, 377 (1970).

[33] D. R. Smith, S. Schultz, P. Markos, and C. M. Soukoulis, Phys. Rev. B **65**, 195104 (2002).
[34] X. Chen, T. M. Grzegorczyk, B. I. Wu, J. Pacheco, Jr., and J. A. Kong, Phys. Rev. E **70**, 016608 (2004).
[35] X. Chen, B. I. Wu, J. A. Kong, and T. M. Grzegorczyk, Phys. Rev. E **71**, 046610 (2005).
[36] C. R. Simovski and S. A. Tretyakov, Phys. Rev. B **75**, 195111 (2007).
[37] C. R. Simovski, Metamaterials **1**, 62 (2007).
[38] A. L. Efros, Phys. Rev. E **70**, 048602 (2004).
[39] R. A. Depine and A. Lakhtakia, Phys. Rev. E **70**, 048601 (2004).
[40] M. G. Silveirinha and C. A. Fernandes, Phys. Rev. E **75**, 036613 (2007).
[41] P. A. Belov and C. R. Simovski, Phys. Rev. B **73**, 045102 (2006).
[42] P. Ikonen, E. Saenz, R. Gonzalo, C. Simovski, and S. Tretyakov, Metamaterials **1**, 89 (2007).
[43] D. M. Pozar, *Microwave Engineering*, 3rd ed. (Wiley, New York, 2005).
[44] S. Tretyakov, *Analytical Modeling in Applied Electromagnetics* (Artech House, Boston, 2003).
[45] T. Koschny, P. Markos, D. R. Smith, and C. M. Soukoulis, Phys. Rev. E **68**, 065602(R) (2003).
[46] G. V. Eleftheriades, O. Siddiqui, and A. K. Iyer, IEEE Microw. Wirel. Compon. Lett. **13**, 51 (2003).
[47] CST Microwave Studio, Darmstadt, Germany.
[48] B. A. Munk, *Frequency Selective Surfaces: Theory and Design* (Wiley, New York, 2000), pp. 2–23.
[49] C. Rockstuhl, T. Paul, F. Lederer, T. Pertsch, T. Zentgraf, T. P. Meyrath, and H. Giessen, Phys. Rev. B **77**, 035126 (2008).
[50] J. Zhou, L. Zhang, G. Tuttle, T. Koschny, and C. M. Soukoulis, Phys. Rev. B **73**, 041101(R) (2006).
[51] C. Caloz, IEEE Microw. Wirel. Compon. Lett. **16**, 585 (2006).
[52] T. Zentgraf, T. P. Meyrath, A. Seidel, S. Kaiser, H. Giessen, C. Rockstuhl, and F. Lederer, Phys. Rev. B **76**, 033407 (2007).
[53] U. K. Chettiar, A. V. Kildishev, H. K. Yuan, W. Cai, S. Xiao, V. P. Drachev, and V. M. Shalaev, Opt. Lett. **32**, 1671 (2007).
[54] M. Kafesaki, I. Tsiapa, N. Katsarakis, Th. Koschny, C. M. Soukoulis, and E. N. Economou, Phys. Rev. B **75**, 235114 (2007).